Tunable Plasmonic Ultrastrong Coupling: Emulating Dicke Physics at Room Temperature

Riad Yahiaoui,[1,*,^] Zizwe A. Chase,[1,^] Chan Kyaw,[1] Fuyang Tay,[2,3] Andrey Baydin,[2,4] G. Timothy Noe II,[2] Junyeob Song,[5] Junichiro Kono,[2,4,6,7] Amit Agrawal,[5,8] Motoaki Bamba,[9,10] and Thomas A. Searles[1,11,*,^]

Affiliations

[1]Department of Physics and Astronomy, Howard University, Washington, DC 20059, USA.
[2]Department of Electrical and Computer Engineering, Rice University, Houston, TX 70005, USA.
[3]Applied Physics Graduate Program, Smalley-Curl Institute, Rice University, Houston, TX 77005, USA.
[4]Smalley-Curl Institute, Rice University, Houston, TX 77005, USA.
[5]Physical Measurement Laboratory, National Institute of Standards and Technology, Gaithersburg, MD 20899, USA.
[6]Department of Physics and Astronomy, Rice University, Houston, TX 77005, USA.
[7]Department of Materials Science and NanoEngineering, Rice University, Houston, TX 77005, USA.
[8]Maryland NanoCenter, University of Maryland, College Park, MD 20742, USA.
[9]The Hakubi Center for Advanced Research, Kyoto University, Kyoto 606-8502, Japan
[10]Department of Physics I, Kyoto University, Kyoto 606-8502, Japan
[11]Department of Physics, Massachusetts Institute of Technology, Cambridge, MA 02139 USA.

*Corresponding authors. Email: riad.yahiaoui@howard.edu (R.Y.); tsearles@mit.edu (T.A.S.)
^Current address: Department of Electrical & Computer Engineering, University of Illinois-Chicago, Chicago, IL, 60607

Abstract

A system of N two-level atoms cooperatively interacting with a photonic field can be described as a single giant atom coupled to the field with interaction strength $\propto \sqrt{N}$. This enhancement, known as Dicke cooperativity in quantum optics, has recently become an indispensable element in quantum information technology based on strong light-matter coupling. Here, we extend the coupling beyond the standard light-matter interaction paradigm, emulating Dicke cooperativity in a terahertz metasurface with N meta-atoms. Cooperative enhancement manifested in the form of matter-matter coupling, through the hybridization of localized surface plasmon resonance in individual meta-atoms and surface lattice resonance due to the periodic array of the meta-atoms. By varying the lattice constant of the array, we observe a clear anticrossing behavior, a signature of strong coupling. Furthermore, through engineering of the capacitive split-gap in the meta-atoms, the coupling rate was cooperatively enhanced into the ultrastrong coupling regime by a factor of $\sqrt{N}$. This room-temperature technology serves as a convenient quantum emulator of the dynamics of a qubit with a giant dipole moment coherently driven by a single bosonic field.

Introduction

The phenomenon of strong coupling (SC) has been observed in various physical systems in recent years and is considered to be a key element in many of the current near-term intermediate-scale quantum information technology such as quantum transduction, networks, and sensing (1). Impressive progress has been made in enhancing the coupling strength from the SC regime and into the ultrastrong coupling (USC) regime (2). The ground state of a system in the USC regime is a highly entangled two-mode squeezed state (3–5), which can be used for efficient protocols for quantum state generation (6), ultrafast two-qubit quantum gates (7, 8), and protected quantum computation, and quantum memories with dramatically enhanced coherence times (9, 10).

The most common mechanism to achieve strong light-matter coupling is by placing an emitter inside a cavity, *i.e.*, a cavity quantum electrodynamics (QED) system. The interaction of cavity photons with the emitter material is usually characterized by two standard parameters: cooperativity $C = 4\Lambda^2/(\kappa\gamma)$, which describes the degree of coherence of the coupling, and the normalized coupling strength ratio $\eta = \Lambda/\omega_0$, where Λ represents the coupling rate proportional to the dipole moment, κ (γ) is the photon (matter) decay rate and ω_0 is the resonance frequency. SC is achieved when $C > 1$ (when the Rabi splitting is larger than the linewidth), and USC is achieved when $\eta \gtrsim 0.1$ (when Λ becomes a considerable fraction of ω_0). To maximize C and Λ/ω_0, one should construct a system that combines a large dipole moment, a small decoherence rate, a large cavity Q factor, and a small resonance frequency.

The coupling rate Λ can be enhanced by a factor of $\sqrt{N}$ when N atoms cooperatively interact with a photonic field (11, 12). This remarkable property, also known as Dicke cooperativity, has recently gained renewed interest in condensed matter cavity QED systems consisting of N dipoles with very large dipole moments (13–16). Most recently, the concept of Dicke physics has been extended to matter-matter coupling, including spin-magnon coupling (17) and magnon-magnon coupling (5). These prior studies, however, have been carried out under conditions that require either low temperatures and/or ultrahigh magnetic fields.

Here, we report a new type of cooperatively enhanced matter-matter USC. We observe cooperative coupling of a localized surface plasmon resonance (LSPR) ensemble with the first-order surface lattice resonance (SLR) in an array of meta-atoms, in the terahertz (THz) frequency range at ambient conditions. The LSPR–SLR coupling rate depicts a characteristic scaling behavior with the density of meta-atoms, evidencing Dicke cooperativity. In this artificial matter–matter system, we simultaneously achieve a high cooperativity $C = 37$ and a normalized coupling strength ratio $\Lambda/\omega_{LSPR} = 0.15$, respectively.

Results

Figure 1A shows the investigated metasurface (MS). It is based on an array of silver (Ag) four-gap split-ring resonators (SRRs) deposited on a 50.8-μm-thick polyimide substrate. The choice of SRRs is of particular interest because of their simple fabrication, full control over the resonance parameters (frequency, linewidth, and amplitude), and room temperature operation. In addition, due to the extreme mechanical flexibility of the substrate, the investigated structure is ideally suited for non-planar applications (18–20). Recently, the use of thin and flexible substrates has provided an unprecedented route to achieve active tunability in the frequency of metamaterials due to modifications in the profiles and the periodicities of the structures when the substrates are stretched (21–23).

The relevant geometrical dimensions of the unit cell are: $R = 90$ μm, $g = 35$ μm, $w = 35$ μm and $p_x = p_y = p$ is varying within the range 275 μm – 400 μm. When $p = 275$ μm, one can observe a dip in transmittance at 0.66 THz, corresponding to the excitation of the localized surface plasmon resonance (LSPR) of individual SRRs (Fig. 1C). The *z-component of the normalized local electric field (E_z)* associated with the LSPR is shown in Fig. 1D and evidences that the electric field is mainly localized around the metal SRRs. More specifically, one can observe a highly confined electric field around the capacitive gaps, and no field enhancement is observed elsewhere, which is one of the bases for high-performance sensing using metafilms [24–26].
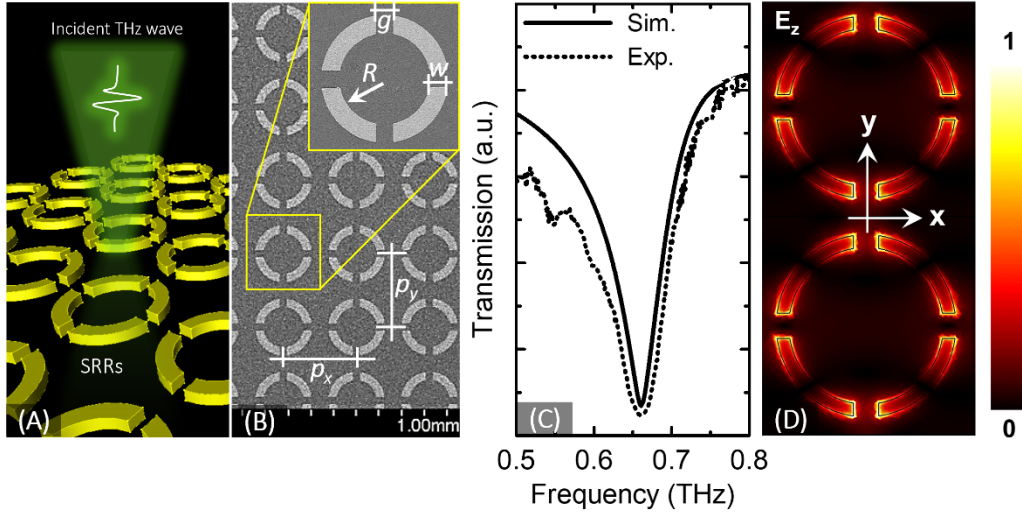

Fig. 1. (A) Schematic of the THz MS array. (B) Scanning electron microscope image (SEM) image of the fabricated sample with the relevant geometrical dimensions: $R = 90$ μm, $g = 35$ μm, $w = 35$ μm and $p = 275$ μm. (C) Simulated (solid line) and measured (dashed line) transmission spectra. (D) Simulated *z-component of the normalized local electric field (E_z)* distribution at the LSPR frequency.

When $p = 275$ μm, the first-order surface lattice resonance (SLR) for the MS sample occurs at a frequency of 0.88 THz and does not couple to the LSPR mode at 0.66 THz. SLRs are typically produced by the interference of a broad resonance, namely LSPR here and a discrete state associated with the light scattered in the plane of the array at the Rayleigh anomaly position (27). Due to simplicity and versatility of the SLR, it has been successfully coupled to different plasmonic systems (28–31). Figure 2A shows the simulated (solid lines) and measured (dotted lines) transmission spectra for different values of the period p (from bottom to top, $p = 275$, 325, 350, 375 and 400 μm, respectively).

For clarity, each curve is vertically offset. Even though there are some differences in amplitudes and bandwidths between simulations and experiments, the measured data confirm very well the numerical predictions, and the general trend is not affected by this discrepancy. The differences between simulations and experiments can be attributed to losses of the substrate, small experimental discrepancies of the geometry from unit cell to unit cell, and residual surface roughness of the samples, which can cause strong inhomogeneous broadening and damping of the resonances (32). At $p = 325$ μm, a resonance additional to the LSPR is observed on the higher frequency side at 0.73 THz, which corresponds to the first-order SLR (Fig. 2A). The corresponding electric field (Fig. 2C) exhibits a simultaneous excitation of the metal SRRs along the polarization direction ($E \parallel$ *x*-axis) and a standing grazing wave in the perpendicular *y*-direction.

Upon increasing the lattice constant of the array from 275 μm to 400 μm and keeping the other geometrical parameters constant, the amplitude, the linewidth, and the spectral position of the resonances are modified (Fig. 2A). The measured transmission spectra are characterized by a transparency window between the two transmission minima. This behavior, named lattice-induced transparency, is analogous to vacuum-Rabi splitting which leads to quantum level repulsion or anti-crossing effect (33, 34). In Fig. 2B, we extract the spectral positions of the two minima from the sample transmission and plot them as a function of lattice constant, which results in upper (UP) and lower (LP) polaritons. As the SLR is varied across the LSPR transition frequency, the system exhibits a distinct anti-crossing feature (Fig. 2B), a clear signature of strong coupling. Numerical simulation, experiment and our quantum model all show good agreement.

The full Hamiltonian of the interacting matter-matter (LSPR–SLR) coupled system can be expressed as (14, 15): $\hat{H}_{\text{tot}} = \hat{H}_{\text{LSPR}} + \hat{H}_{\text{SLR}} + \hat{H}_{\text{int}} + \hat{H}_{A^2}$, where $\hat{H}_{\text{LSPR}} = \hbar\omega_{LPR}\hat{a}^\dagger\hat{a}$, $\hat{H}_{\text{SLR}} = \hbar\omega_{\text{SLR}}\hat{b}^\dagger\hat{b}$ and $\hat{H}_{\text{int}} = \hbar\Lambda\hat{a}(\hat{b}^\dagger - \hat{b}) + \hbar\Lambda\hat{a}^\dagger(\hat{b}^\dagger - \hat{b})$ and $\hat{H}_{A^2} = (\hbar\Lambda^2/\omega_{\text{SLR}})(\hat{a}^\dagger\hat{a}^\dagger + \hat{a}^\dagger\hat{a} + \hat{a}\hat{a}^\dagger + \hat{a}\hat{a})$. The first two terms $\hat{H}_{LSPR}$ and $\hat{H}_{SLR}$ represent the energy of the LSPR at ω_{LSPR} and the energy of the SLR at ω_{SLR}. The operators $\hat{a}$ and $\hat{a}^\dagger$ ($\hat{b}$ and $\hat{b}^\dagger$) are the annihilation and creation operators for LSPR (SLR), respectively. The matter-matter interaction term, $\hat{H}_{\text{int}}$, with coupling strength Λ includes counter-rotating terms, $\hbar\Lambda(\hat{a}^\dagger\hat{b}^\dagger - \hat{a}\hat{b})$, which are usually neglected under the rotating wave approximation. Also included in the total Hamiltonian is the so-called A^2 term. The pre-factor $\hbar\Lambda^2/\omega_{\text{SLR}}$ of the A^2 term suggests that this term is negligible in the weak-coupling regime, but can have measurable effects when Λ is a significant fraction of ω_{SLR}.

Strongly coupled systems exchange energy among the modes, quantified by the vacuum-field Rabi splitting frequency. Solid white lines in Figure 2B present the best fit to our data. The vacuum Rabi frequency Ω_{R}, which is defined as the frequency separation of the two polariton branches at zero detuning (*i.e.*, when the uncoupled LSPR and SLR frequencies are equal) was determined to be 50 GHz at p = 348 μm, is equal to twice the LSPR–SLR coupling strength Λ. This corresponds to a normalized coupling strength ratio $\Lambda/\omega_{\text{LSPR}}$ of 3.79 %, which is similar to the recently reported threshold in the THz frequency regime (30).

To achieve SC with N emitters at room temperature, the coupling strength $\Lambda \propto \sqrt{N/V}$ needs to exceed the cavity loss rate $\kappa \propto 1/Q$ and the total emitter decay rate γ (35). This can be achieved by reducing the mode volume in plasmonic resonators and by using large numbers of emitters. In this context, periodic MSs with subwavelength features offer a remarkable alternative to the standard cavity scheme. Figure 3 shows that by actively changing the capacitive gap of the SRR array, it is possible to dynamically tune and enhance the normalized coupling strength ratio. Indeed, as the capacitive split gap g is decreased from 35 μm to 5 nm, a blueshift and detuning of the polaritonic curves occurs, which is accompanied by a gradual enhancement of the normalized coupling strength ratio ($\Lambda/\omega_{\text{LSPR}}$).
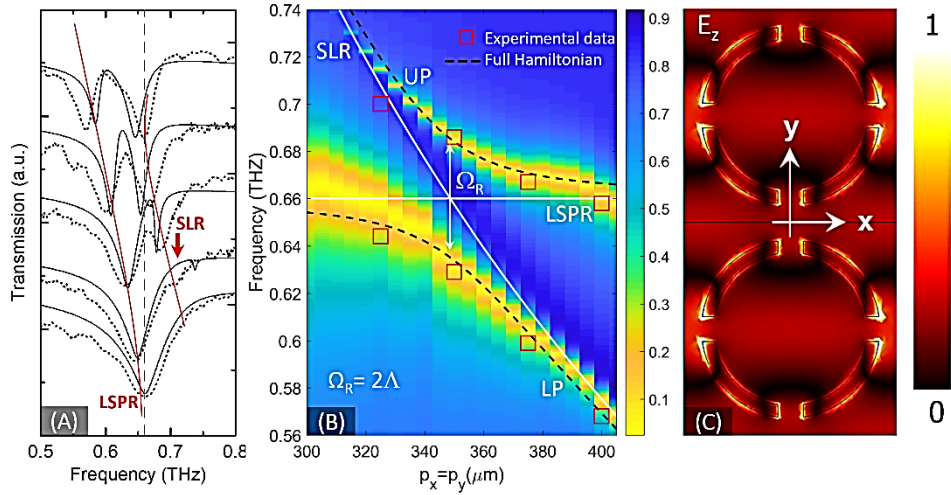
Figure 2. (A) Simulated (solid line) and measured (dashed line) transmission spectra of the Metasurface for different lattice constants p. From bottom to top, p = 275, 325, 350, 375 and 400 μm, respectively. The spectra are offset vertically for clarity. The red lines are guides to the eye and follow the position of the two polaritonic states. (B) The extracted frequencies versus lattice constant p are displayed of the simulated and measured resonances, showing an anti-crossing behavior (vacuum Rabi splitting $\Omega_R(g) = 2\Lambda$). (C) Simulated *z-component of the normalized local electric field (E_z)* distribution at the frequency of the first-order SLR for an intermediate periodicity of p = 350 μm.

Notably, the system exhibits the largest normalized coupling strength ratio Λ/ω_{LSPR} when g = 5 nm, corresponding to an equivalent total capacitance C_T of about 7.32 fF. Indeed, at zero detuning where $\omega_{LSPR} = \omega_{SLR}$ = 0.415 THz (at p = 554.4 μm), the measured polariton mode splitting 2Λ = 120 GHz, which yields a normalized coupling strength ratio of 0.15 (Figs. 3F and 3G, respectively); this puts the system into the USC regime, defined by $\Lambda/\omega_{LSPR} > 0.1$ (16). The damping rates for the LSPR (κ = 13.34 GHz) and SLR (γ = 29.12 GHz), derived from the data in Fig. 2B (fitted blue dashed curve) and Fig. 1B, respectively, one calculates a cooperativity factor C = 37. This value indicates that the system reaches the USC regime. The coupling strength ratio can be further enhanced through a more exotic design of the resonators.

The *results obtained* here *clearlydemonstrate* that the equivalent capacitance associated with the metallic resonators is a crucial parameter determining the coupling strength Λ. As a result, increasing the capacitance of the metamaterial resonator increases the Rabi frequency. Similar capacitance-dependence of the Rabi splitting was observed in a metamaterial nanocavity coupled to intersubband transitions in a semiconductor heterostructure quantum well (QW) (36).

Interestingly enough, we also found the magnitude of the coupling rate $\tilde{\Lambda}$ to be proportional to $\alpha\sqrt{\rho}$, illustrating the collective nature of the LSPR–SLR coupling, where ρ is the surface density of the MS unit cells and α is a fitting parameter, which is set to a = 0.5 (Fig. 4). The situation is analogous to a standard *N*-atom cavity QED experiment, in which an ensemble of *N* two-level atoms couples with a vacuum photon field in an optical cavity. Here, we extended the concept of cooperatively enhanced coupling to an exclusively solid-state system, demonstrating that it also occurs in artificial plasmonic meta-atoms in the form of matter-matter interaction.
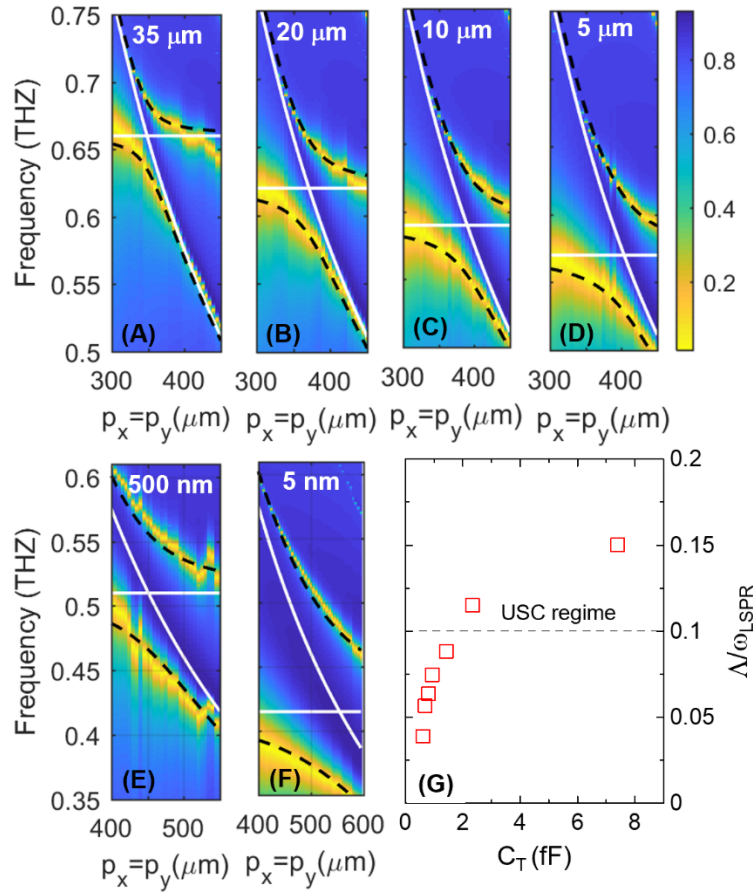
Figure 3. **Capacitance-dependent anti-crossing spectra for the metasurface.** (A)-(F) Contour plots illustrating the transmission amplitude for different values of the capacitive gap g between 5 nm and 35 μm. A full Hamiltonian is used here to fit the numerical data. The white solid lines represent the LSPR and SLR transmission dip positions, respectively. (G) Evolution of the normalized coupling strength ratio vs the equivalent total capacitance of the metasurface. We observed a clear capacitance-dependent LSPR–SLR anticrossing behavior (Fig. 3, A to F), and the magnitude of Λ/ω_{LSPR} increases with decreasing split capacitive gap, indicating that the LSPR–SLR coupling becomes stronger.

From the contour plot spectrum of Fig. 3A (when g = 35 μm), we determined the total capacitance C_T = 0.46 fF, the periodicity at zero detuning p = 348 μm and the corresponding surface density of the MS unit cells ρ = 7.5 ×10^6 /m^2, yielding to Ω_R = 50 GHz and Λ/ω_{LSPR} = 0.0379. Parameter values determined in this manner for all capacitive split gaps are summarized in Table 1.
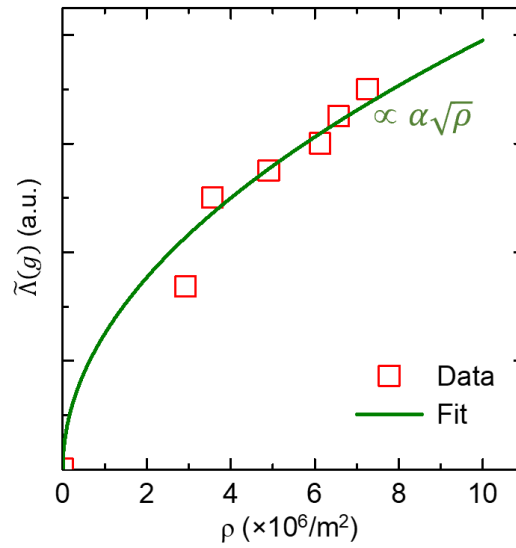
Figure 4. **Dependence of Rabi splitting on SRR unit cell density.** The red squares show the coupling rate obtained with a single MS layer, while the green solid line represents a square-root fit.

g(μm)	C_T(fF)	p(μm) at anti-crossing	$\rho(10^6/m^2)$	n_{eff}	Ω_R(GHz)	$\Omega_R/(2\omega_{LSPR})$	$\dfrac{\Omega_R n_{eff}}{2\sqrt{\frac{C_T(g)-C_{rest}}{C_{ref}}}\omega_{LSPR}(g)\omega_{ref}}$
35	0.46	348	7.58	1.3	50	0.0060	0.0012
20	0.57	371.12	7.26	1.3	70	0.0090	0.0014
10	0.71	389.98	6.57	1.3	75	0.0101	0.0013
5	0.85	403.68	6.13	1.3	85	0.0119	0.0012
0.5	1.35	451.16	4.91	1.3	90	0.0140	0.0011
0.05	2.26	538.54	3.57	1.3	100	0.0183	0.0010
0.005	7.32	554.43	2.93	1.3	120	0.1500	0.000672

Table 1. Parameters extracted for each capacitive split-gap discussed in the main text.

Discussion

Here we provide some interpretations to several findings presented in the results section. First, it is well known that the arrangement of metallic micro/nanoparticles into a periodic lattice can give rise to an in-plane propagating lattice surface mode, which appears near the Wood anomaly (37). The wavelength of the Wood anomaly can be calculated by matching the wave vector k_{in} of incident light in the surrounding air medium with the reciprocal vector $G_{i,j}$ of a two-dimensional square lattice. According to grating theory, in the most general case of a square grating with period p sitting on the interface between two media with refractive indices n_1 and n_2, the position of the Rayleigh anomalies is given by (27):

$$\lambda_{i,j} = p\frac{\sqrt{n_2^2(i^2+j^2)-n_1^2 j^2\sin^2\theta}\pm in_1\sin\theta}{i^2+j^2} \tag{1}$$

where θ is the angle of incidence, and i and j are integers corresponding to the diffracted order of the anomaly. Under normal incidence (*i.e.*, $\theta = 0°$), the condition for the excitation of the SLR for an effective square lattice in the surrounding air medium ($n_1 = 1$) can be thus simplified by

$$\lambda_{i,j} = p \frac{\sqrt{n_{\text{eff}}^2 (i^2+j^2)}}{i^2+j^2} \tag{2}$$

From simulation results, the effective refractive index $n_2 = n_{\text{eff}}$ was deduced to be about 1.3. By varying the lattice constant of the meta-atoms to greater spacings, we continuously changed the detuning between the SLR and the LSPR, which provides a possibility for the SLR to coincide with and couple to the fundamental radiative LSPR at a certain range of periodicities. The possibility to continuously tune the SLR allows to follow the evolution of the polaritonic states (one can clearly see the interaction of the two modes), as the system is driven from the uncoupled regime to the strongly coupled one. Indeed, as shown in Fig. 2, for a periodicity of $p = 325$ μm, a weak coupling occurs between the LSPR and the SLR of the SRRs with a gap width of $g = 35$ μm. Upon increasing the periodicity to $p = 348$ μm, the SLR mostly overlaps with the LSPR, thus leading to the formation of two mixed modes as a result of the strong coupling. When the periodicity is further increased to $p = 400$ μm, the SLR is resonant out of the LSPR, and only weak coupling between these two resonances is observed (Fig. 2).

1. Capacitively-assisted Rabi splitting enhancement

Our aim is to understand the correlation between the geometry of SRRs, particularly the capacitive split gap g, and the enhancement of the coupling rate Λ observed in Fig. 3. One advantage of the metasurface-based plasmonic systems is the ability to localize strong field concentrations within small split-gaps when excited by incident light and dramatically enhance nonlinear response in materials being introduced. To gain a deeper insight into the physics of the capacitively-mediated enhanced coupling rate, we plotted in Fig. 5 the dependence of the z–component electric field (E_z) enhancement on the total capacitance C_T.

One can observe that decreasing the size of the split gap in the deep subwavelength scale (i.e., $\ll \lambda_0$), namely from 35 μm to 5 nm, causes remarkable local field enhancement at the split gap of the SRRs. Indeed, an increase of about 15-fold is achieved for a 5 nm gap. The field enhancement (light localization) in the gaps of the resonators can be explained microscopically by opposite charges accumulation at the two sides of the gap. Therefore, stronger field enhancement can be realized with a shorter gap. The presence of the substrate affects the electric field enhancement and increases the effective width of the gap. This causes a blueshift of the frequency of resonance and reduces the field concentration. So, a substrate with a low refractive index is preferred for strong field enhancement (38).

Additionally, it is found that the linewidth of the uncoupled LSPR is systematically broadened as the equivalent total capacitance increases (g decreases), namely $Q \approx 2.23$ for an intermediate $g = 50$ nm ($g \approx \lambda_0/10^5$), as compared with $Q = 11.46$ for $g = 35$ μm ($g \approx \lambda_0/14$, from Fig. 1B), both estimated when $p = 300$ μm. This broadening of the linewidth, which results from a *radiative damping* process, indicates that the incident light propagates with *high* scattering, suggesting a strong diffraction coupling, similar to the functioning of a diffraction grating based on subwavelength apertures array. Consequently, the normalized coupling strength ratio $\Lambda/\omega_{\text{LSPR}}$ between the SLR and the LSPR is dramatically enhanced so that the USC regime is reached.
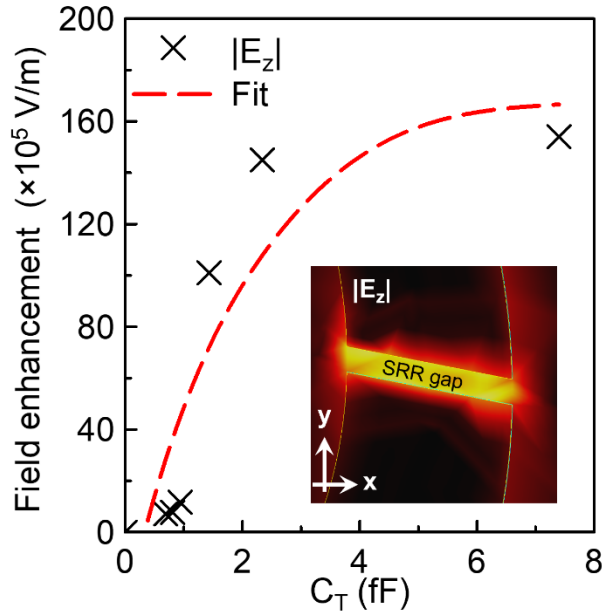
Figure 5. **Dependence of the maximum field enhancement factor on gap size**. Electric field enhancements calculated at the x–y plane of $z = 0$ μm for different gap widths. the dashed red curve is a fitted line. Inset: *z-component of the normalized electric field (E$_z$) distribution at zero detuning for the MS with a gap width of g = 500 nm.*

2. Cooperatively enhanced strong coupling

We demonstrated that the coupling rate exhibits a square-root dependence on the density of the MS unit cells, proving the collective interaction of an ensemble of dipoles. To extract more quantitative information from our data, we developed a model based on the light-matter coupling theory and circuit network theory as follows. According to (39), the LM-LSPR coupling strength Λ should be expressed as

$$\Lambda(g, p_x, p_y) = \sqrt{\frac{\omega_{\mathrm{LSPR}}(g)N}{2\hbar\epsilon_0\epsilon_{\mathrm{eff}}(g)}} \frac{d(g)}{\sqrt{V(p_x,p_y)}}. \quad (3)$$

Here, we assume that $\Lambda(g, p_x, p_y)$ depends on the capacitive gap g, periods p_x and p_y of the ring array. The LSPR (angular) frequency $\omega_{\mathrm{LSPR}}(g)$ depends on g. N is the number of rings in the whole system. $\hbar$ is the Planck constant. ϵ_0 is the vacuum permittivity. $\epsilon_{\mathrm{eff}}(g) = n_{\mathrm{eff}}(g)^2$ is the relative permittivity for the SLR depending on the capacitive gap g. The SLR frequency is expressed as

$$\omega_{SLR}(g, p_x, p_y) = \frac{c}{n_{\mathrm{eff}}(g)} \frac{2\pi}{\lambda_{\mathrm{eff}}(p_x,p_y)}. \quad (4)$$

Here, c is the speed of light in the vacuum. $\lambda_{\mathrm{eff}}(p_x, p_y) = p \times n_{eff}$ is the effective wavelength of the SLR. In Eq. (3), $d(g)$ is the g-dependent transition dipole moment of each ring. $V(p_x, p_y) = Np_x p_y w$ is the volume of the SLR, where w is the effective width.

On the other hand, in the context of the circuit network theory, the SRR is assumed to be equivalent to a resonant LC circuit model, where the split gap corresponds to the capacitive term "C" and the SRR loop corresponds to the inductive term "L". $\omega_{\mathrm{LSPR}}(g) = 1/\sqrt{LC_{\mathrm{LSPR}}(g)}$ represents the LSPR frequency with the g-dependent capacitance $C_{\mathrm{LPR}}(g)$ relevant to the LSPR frequency [see the Supplementary Materials for details]. The SLR with frequency ω_{SLR} can also be treated as an LC circuit in the network theory. When the SLR and the LSPR ensemble are coupled capacitively (through a coupling capacitance C_c), the coupling Hamiltonian is typically expressed as (40):

$$\hat{H}_{\text{int}} = \sum_{j=1}^{N} \frac{\hat{Q}\hat{q}_j}{C_c}. \qquad (5)$$

Here, $\hat{Q}$ is the operator of charge in the SLR circuit and $\hat{q}_j$ is that in the j-th LSPR circuit. When we introduce annihilation (creation) operators of the SLR and j-th LSPR as $\hat{a}$ ($\hat{a}^\dagger$) and $\hat{\beta}_j$ ($\hat{\beta}_j^\dagger$), respectively, the charge operators are represented as

$$\hat{Q} = \sqrt{\frac{\hbar}{2Z_{\text{SLR}}}}(\hat{a}^\dagger + \hat{a}), \qquad (6)$$

$$\hat{q}_j = \sqrt{\frac{\hbar}{2Z_{\text{LSPR}}}}(\hat{\beta}_j^\dagger + \hat{\beta}_j). \qquad (7)$$

Here, Z_{SLR} and Z_{LSPR} are the impedance of the SLR and LSPR circuits, respectively. The latter can be rewritten by the inductaince L, capacitance C_{LSPR}, and ω_{LSPR} as $Z_{\text{LSPR}} = 1/(\omega_{\text{LSPR}}C_{\text{LSPR}})$. Thus, the coupling Hamiltonian in Eq. (5) can be rewritten as

$$\hat{H}_{\text{int}} = \sum_{j=1}^{N} \frac{\hbar}{2C_c}\sqrt{\frac{\omega_{\text{LSPR}}C_{\text{LSPR}}}{Z_{\text{SLR}}}}(\hat{a}^\dagger + \hat{a})(\hat{\beta}_j^\dagger + \hat{\beta}_j). \qquad (8)$$

$$\hat{H}_{\text{int}} = \frac{\hbar}{2C_c}\sqrt{\frac{\omega_{\text{LSPR}}C_{\text{LSPR}}N}{Z_{\text{SLR}}}}(\hat{a}^\dagger + \hat{a})(\hat{b}^\dagger + \hat{b}). \qquad (9)$$

Here, we defined the annihilation operator of the collective dipole excitation as

$$\hat{b} \equiv \sum_{j=1}^{N} \frac{\hat{\beta}_j}{\sqrt{N}}. \qquad (10)$$

Thus, the coupling strength is expressed as

$$\Lambda = \frac{1}{2C_c}\sqrt{\frac{\omega_{\text{LSPR}}C_{\text{LSPR}}N}{Z_{\text{SLR}}}}. \qquad (11)$$

Comparing with Eq. (3), because ϵ_{eff} and V are parameters of the SLR, we can find that the transition dipole moment $d(g)$ in Eq. (3) should be proportional to $\sqrt{C_{\text{LSPR}}(g)}$. We consider that the total capacitance $C_{\text{T}}(g)$ consists of $C_{\text{LSPR}}(g)$ and others C_{rest} as $C_{\text{T}}(g) = C_{\text{LSPR}}(g) + C_{\text{rest}}$. The transition dipole is then expressed as

$$d(g) = \eta\sqrt{C_{\text{LSPR}}(g)} = \eta\sqrt{C_{\text{T}}(g) - C_{\text{rest}}}. \qquad (12)$$

with a factor η.

Using this relation between the transition dipole moment $d(g)$ and capacitance $C_T(g)$ or $C_{\text{LSPR}}(g)$ derived from the circuit network theory, Eq. (3) is rewritten as

$$\frac{\Lambda(g,p_c(g),p_c(g))n_{\text{eff}}(g)}{\sqrt{C_{\text{LSPR}}(g)\omega_{\text{LSPR}}(g)}} = \frac{\eta}{\sqrt{2\hbar\epsilon_0 w}}\sqrt{\rho(g)}. \qquad (13)$$

In Fig. 3, we calculated the resonance frequencies of the whole system as functions of the periods $p_x = p_y$ for a fixed capacitive gap g. At each crossing point $p_x = p_y = p_c(g)$ giving $\omega_{\text{LSPR}}(g) = \omega_{\text{SLR}}(g,p_c(g),p_c(g))$, we got an anti-crossing (vacuum Rabi splitting) frequency $\Omega_{\text{R}}(g) = 2\Lambda(g,p_c(g),p_c(g))$. We also got the effective refractive index $n_{\text{eff}}(g) = \sqrt{\epsilon_{\text{eff}}(g)}$ by the gradient of the SLR frequency against $p_x = p_y$ through Eq. (4). The surface density $\rho(g) \equiv 1/p_c(g)^2$ at the crossing point is also determined. They are summarized in Table 1. Substituting $\Lambda(g,p_c(g),p_c(g)) = \Omega_{\text{R}}(g)/2$ and $C_{\text{LSPR}}(g) = C_{\text{T}}(g) - C_{\text{rest}}$ into Eq. (13) and introducing reference capacitance $C_{\text{ref}} = 0.46$ fF and reference frequency $\omega_{ref}/2\pi = 0.66$ THz, we define a dimensionless coupling strength

$$\tilde{\Lambda}(g) \equiv \frac{\Omega_{\text{R}}(g)n_{\text{eff}}(g)}{2\sqrt{\frac{C_{\text{T}}(g) - C_{\text{rest}}}{C_{ref}}\omega_{\text{LSPR}}(g)\omega_{ref}}} = \eta\sqrt{\frac{C_{ref}}{2\hbar\epsilon_0 w\omega_{ref}}}\sqrt{\rho(g)}. \qquad (14)$$

In Fig. 4, we plotted the left-hand side of Eq. (14) as a function of density $\rho(g)$. One clearly notices that the data indeed exhibit a square-root dependence, evidencing the collective interaction of a dilute ensemble of dipoles (38).

Conclusions

We have demonstrated ultrastrong coupling in a free-standing single-layer THz MS at room temperature. This phenomenon manifests in the form of matter-matter coupling, involving the hybridization of localized surface plasmon resonance (LSPR) and surface lattice resonance (SLR) in an array of N artificial meta-atoms, namely SRRs. Driven by the inter meta-atom distance and judiciously assisted by a capacitive split-gap adjustment of the SRRs, the coupling rate was cooperatively enhanced into the ultrastrong coupling regime by a factor of $\sqrt{N}$. This highly tunable room-temperature system can be viewed as a macroscopic quantum emulator of the dynamics of a single qubit with a giant dipole moment coherently driven by a single bosonic field. Moreover, one can envisage hybrid cavities, where the plasmon-plasmon polaritons additionally couple to fermionic material systems, such as quantum wells or superconductor qubits for potential quantum information processing.

Materials and methods

Numerical calculations were performed using the finite-difference time-domain (FDTD) method to predict the spectral response of the structure. In these calculations, the unit cell of the MS is illuminated at normal incidence, under a linearly TM-polarized wave ($E \parallel x$-axis). The incident light is a plane wave impinging from the substrate side. Due to the rotational symmetry imposed by the geometry of the design, the structure has an identical response for an incident TE-polarized radiation (i.e., $E \parallel y$-axis). Periodic boundary conditions are applied to mimic a two-dimensional (2D) infinite structure. The length scale of the mesh was set to be less than or equal to $\lambda_0/10$ throughout the simulation domain, where λ_0 is the central wavelength of the incident radiation. The input and output ports are located at about $3\lambda_0$ from the MS with open boundary conditions. The polyimide film is treated as a dielectric with $\varepsilon = 3.3 + i0.05$, and the metallic Ag layer is modeled as a lossy metal with a conductivity of 4.1×10^7 S/m.

Experimental prototypes with an active sample area of 1.5 cm × 1.5 cm were fabricated using standard photolithography and deposition of 100 nm of Ag with a 10 nm thick adhesive layer of chromium (Cr) on a flexible 50.8-μm-thick polyimide film followed by lift-off to remove the excess metal.

Measurements are performed using a continuous-wave (CW) THz spectrometer (TeraScan 1550 radiation source from Toptica) that produces a linearly polarized collimated terahertz beam with a spectral resolution < 2 GHz. In this system, the optical beat frequency of two distributed feedback (DFB) diode lasers is tuned to produce coherent THz waves between 0 and 1.8 THz. The THz wave is detected by an InGaAs photoconductive antenna with phase-sensitive photocurrent acquisition. The transmission from each sample is calculated as $T(\omega) = P_{\mathrm{MS}}(\omega) / P_{\mathrm{sub}}(\omega)$, where $P_{\mathrm{MS}}(\omega)$ and $P_{\mathrm{sub}}(\omega)$ are the transmitted power spectra of the planar MS and substrate, respectively.

References and notes

1. D. Awschalom *et al.,* Development of Quantum Interconnects (QuICs) for next-generation information technologies. *PRX Quantum*, **2**, 017002 (2021).
2. P. Forn-Díaz, L. Lamata, E. Rico, J. Kono, E. Solano, Ultrastrong coupling regimes of light-matter interaction. *Rev. Mod. Phys*. **91**, 025005 (2019).
3. C. Ciuti, G. Bastard, I. Carusotto, Quantum vacuum properties of the intersubband cavity polariton field. *Phys. Rev. B* **72**, 115303 (2005).
4. S. Ashhab, F. Nori, Qubit-oscillator systems in the ultrastrong-coupling regime and their potential for preparing nonclassical states. *Phys. Rev. A* **81**, 042311 (2010).
5. T. Makihara et al., Ultrastrong magnon–magnon coupling dominated by antiresonant interactions. *Nat. Commun*. **12**, 3115 (2021).
6. Y.-D. Wang, S. Chesi, D. Loss, C. Bruder, One-step multiqubit Greenberger-Horne-Zeilinger state generation in a circuit QED system. *Phys. Rev. B* **81**, 104524 (2010).
7. G. Romero, D. Ballester, Y. M. Wang, V. Scarani, E. Solano, Ultrafast quantum gates in circuit QED. *Phys. Rev. Lett.* **108**, 120501 (2012).
8. T. H. Kyaw, D. A. Herrera-Martí, E. Solano, G. Romero, L.-C. Kwek, Creation of quantum error correcting codes in the ultrastrong coupling regime. *Phys. Rev. B* **91**, 064503 (2015).
9. P. Nataf, C. Ciuti, Protected quantum computation with multiple resonators in ultrastrong coupling circuit QED. *Phys. Rev. Lett.* **107**, 190402 (2011).
10. T. H. Kyaw, S. Felicetti, G. Romero, E. Solano, L.-C. Kwek, Scalable quantum memory in the ultrastrong coupling regime. *Sci. Rep*. **5**, *8621* (*2015*).
11. R. H. Dicke, Coherence in spontaneous radiation processes. *Phys. Rev*. **93**, 99–110 (1954).
12. M. Tavis, F. W. Cummings, Exact solution for an N-molecule-radiation-field Hamiltonian. *Phys. Rev*.,**170**, *379*–384 (*1968*).
13. Y. Tabuchi, S. Ishino, T. Ishikawa, R. Yamazaki, K. Usami, and Y. Nakamura, Hybridizing Ferromagnetic Magnons and Microwave Photons in the Quantum Limit. *Phys. Rev. Lett.* **113**, 083603 (2014).
14. Q. Zhang, M. Lou, X. Li, J. L. Reno, W. Pan, J. D. Watson, M. J. Manfra, J. Kono, Collective non-perturbative coupling of 2D electrons with high-quality-factor terahertz cavity photons. *Nature Phys* **12**, 1005–1011 (2016).
15. X. Li, M. Bamba, Q. Zhang, S. Fallahi, G. C. Gardner, W. Gao, M. Lou, K. Yoshioka, M. J. Manfra, Junichiro Kono, Vacuum Bloch–Siegert shift in Landau polaritons with ultra-high cooperativity. *Nature Photon* **12**, 324–329 (2018).
16. W. Gao, X. Li, M. Bamba, J. Kono, Continuous transition between weak and ultrastrong coupling through exceptional points in carbon nanotube microcavity exciton–polaritons. *Nature Photon* **12**, 362–367 (2018).
17. X. Li, M. Bamba, N. Yuan, Q. Zhang, Y. Zhao, M. Xiang, K. Xu, Z. Jin, W. Ren, G. Ma, S. Cao, D. Turchinovich, J. Kono, Observation of Dicke cooperativity in magnetic interactions. *Science* **361**, 794–797 (2018).
18. R. Yahiaoui, K. Takano, F. Miyamaru, M. Hangyo, and P. Mounaix, Terahertz metamolecules deposited on thin flexible polymer: design, fabrication and experimental characterization. *J. Opt.* **16**, 094014 (2014).
19. H. Tao, A. C. Strikwerda, K. Fan, C. M. Bingham, W. J. Padilla, X. Zhang, and R. D. Averitt, Terahertz metamaterials on free-standing highly flexible polyimide substrates. *J. Phys. D* **41**, 232004 (2008).
20. R. Yahiaoui, J. P. Guillet, F. de Miollis, and P. Mounaix, Ultra-flexible multiband terahertz metamaterial absorber for conformal geometry applications. *Opt. Lett.* **38**, 4988–4990 (2013).

21. S. Lee, S. Kim, T. Kim, Y. Kim, M. Choi, S. H. Lee, J. Kim, B. Min, Reversibly stretchable and tunable terahertz metamaterials with wrinkled layouts. *Adv. Mater*. **24**, 3491–3497 (2012).

22. J. Li, C. M. Shah, W. Withayachumnankul, B. Ung, A. Mitchell, S. Sriram, M. Bhaskaran, S. Chang, D. Abbott, Mechanically tunable terahertz metamaterials. *Appl. Phys. Lett*. **102**, 121101 (2013).

23. F. Zhang, S. Feng, K. Qiu, Z. Liu, Y. Fan, W. Zhang, Q. Zhao, and J. Zhou, Mechanically stretchable and tunable metamaterial absorber. *Appl. Phys. Lett.* **106**, 091907 (2015).

24. L. Cong, S. Tan, R. Yahiaoui, F. Yan, W. Zhang, and R. Singh, Experimental demonstration of ultrasensitive sensing with terahertz metamaterial absorbers: A comparison with the metasurfaces. *Appl. Phys. Lett.* **106**, 031107 (2015).

25. R. Yahiaoui, S. Tan, L. Cong, R. Singh, F. Yan, and W. Zhang, Multispectral terahertz sensing with highly flexible ultrathin metamaterial absorber. *J. Appl. Phys.* **118**, 083103 (2015).

26. R. Yahiaoui, A. C. Strikwerda, and P. U. Jepsen, Terahertz plasmonic structure with enhanced sensing capabilities. *IEEE Sens. J.* **16**, 2484–2488 (2016).

27. R. W. Wood, On the remarkable case of uneven distribution of a light in a diffraction grating spectrum. *Philos. Mag*. **4**, 396–402 (1902).

28. T. C. Tan, Y. K. Srivastava, M. Manjappa, E. Plum, R. Singh, Lattice induced strong coupling and line narrowing of split resonances in metamaterials. *Appl. Phys. Lett*. **112**, 201111 (2018).

29. A. Bitzer, J. Wallauer, H. Helm, H. Merbold, T. Feurer, M. Walther, Lattice modes mediate radiative coupling in metamaterial arrays. *Opt. Express*, **17**, 22108–22113 (2009).

30. J. Keller, C. Maissen, J. Haase, G. L. Paravicini-Bagliani, F. Valmorra, J. Palomo, J. Mangeney, J. Tignon, S. S. Dhillon, G. Scalari, J. Faist. Coupling Surface Plasmon Polariton Modes to Complementary THz Metasurfaces Tuned by Inter Meta-Atom Distance. *Adv. Opt. Mater*. **5**, 1600884 (2017).

31. P. Klarskov, A. T. Tarekegne, K. Iwaszczuk, X.-C. Zhang, P. U. Jepsen, Amplification of resonant field enhancement by plasmonic lattice coupling in metallic slit arrays. *Sci Rep* **6,** 37738 (2016).

32. J. A. Burrow, R. Yahiaoui, A. Sarangan, I. Agha, J. Mathews, T. A. Searles, Polarization-dependent electromagnetic responses of ultrathin and highly flexible asymmetric terahertz metasurfaces. *Opt. Express* **25**, 32540–32549 (2017).

33. M. Manjappa, Y. K. Srivastava, R. Singh, Lattice-induced transparency in planar metamaterials. *Phys. Rev. B*, **94**, 161103 (2016).

34. J. A. Burrow, R. Yahiaoui, A. Sarangan, J. Mathews, I. Agha, T. A. Searles, Eigenmode hybridization enable lattice-induced transparency in symmetric terahertz metasurfaces for slow light applications. *Opt. Lett.* **44**, 2705–2708 (2019).

35. H. Groß, J. M. Hamm, T. Tufarelli, O. Hess, B. Hecht, Near-field strong coupling of single quantum dots. *Sci. Adv*. **4**, r4906 (2018).

36. A. Benz, S. Campione, J. F. Klem, M. B. Sinclair, I. Brener, Control of strong light-matter coupling using the capacitance of metamaterial nanocavities. *Nano Lett*. **15**, 1959–1966 (2015).

37. F. J. García de Abajo, Colloquium: Light scattering by particle and hole arrays. *Rev. Mod. Phys*. **79**, 1267-1290 (2007).

38. F. Meng, M. D. Thompson, B. Klug, D Čibiraitè, Q. Ul-Islam, H. G. Roskos, Nonlocal collective ultrastrong interaction of plasmonic metamaterials and photons in a terahertz photonic crystal cavity. *Opt. Express* **27**, 24455–24468 (2019).

39. N. M. Peraca, A. Baydin, W. Gao, M. Bamba, J. Kono, Ultrastrong light-matter coupling in semiconductors. In *Semicond. Quantum Sci. Technol.*, **105**, 89–151 (2020). Elsevier, Cambridge, SanDiego, Oxford, London, 2020.
40. V. E. Manucharyan, A. Baksic, and C. Ciuti, Resilience of the quantum Rabi model in circuit QED. *J. Phys. A: Math. Theor.,* **50**, 294001 (2017).

Supplementary Materials for

Tunable Plasmon-Plasmon Ultrastrong Coupling: Emulating Dicke Physics at Room Temperature

Equivalent circuit model

Features of the fundamental localized surface plasmon resonance (LSPR) of the split ring resonator (SRR) can be understood by considering an equivalent circuit model, where the split gap can be regarded as a capacitor C, the SRR loop corresponds to the inductive term "L" and the resistance of the metal as a resistor R (Figure S1). The total impedance Z is given as follows:

$$Z = R + 2\pi i f L + \frac{1}{2\pi i f C} \tag{1}$$

The resonance occurs when the total impedance is minimized. Considering that the change of R in the THz range is relatively small, the resonance frequency is approximately $f_{res} \approx 1/(2\pi\sqrt{LC})$. The analytical expression for the total capacitance C consists of the gap C_{gap} and surface capacitances C_{surf}. If the gap is narrow its capacitance can be written as

$$C_{gap} = \varepsilon_0 \frac{h\omega}{g} + C_0 \tag{2}$$

where ε_0 is the free-space permittivity. The first term on the right-hand side is the usual expression for the parallel-plate capacitor formed by the gap and the second term is a correction due to the fringing fields. C_0 is calculated as follows:

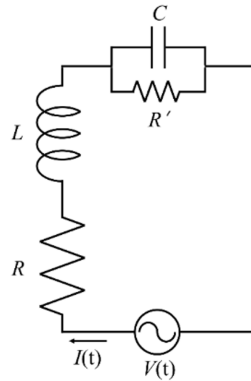$$C_0 = \varepsilon_0(h + w + g) \tag{2}$$

Figure S1. Circuit modelling of the split ring resonator unit cell.

The surface capacitance per unit height is determined as following. In the vicinity of a small gap, R_g, the split ring will look like that shown in Fig. S1. The surfaces of the split ring can be presented by two planes along the x-axis. Assuming the planes to be infinitely long and

infinitely thin, the problem is reduced to that of 2D electrostatics. The complex electric field $E(x,y) = E_x + iE_y$ can be then found using conformal mapping as (1):

$$E = \frac{2V_0}{g\pi} \overline{\left[1 - \left(\frac{2z}{g}\right)^2\right]^{-1/2}} \tag{3}$$

where $z = x + iy$; i is the complex unity, and the bar means complex conjugation. The electric field lines are ellipses as shown schematically in Fig. S2. The surface charge density is proportional to the y-component of the electric field in the plane $x = 0$.

$$\sigma = \frac{4\varepsilon_0 V_0}{g\pi} \frac{1}{\sqrt{\left(\frac{2y}{g}\right)^2 - 1}} \tag{4}$$

The linear charge density is then

$$\lambda = \int_{g/2}^{\infty} \sigma \, dy = \frac{2\varepsilon_0 V_0}{\pi} \int_1^{\infty} \frac{dy}{\sqrt{y^2 - 1}} \tag{5}$$

This integral does not converge at infinity; its upper limit should be changed to a large but finite number. Since we assumed that $R \gg g$, it is natural to take R/g as the upper limit

$$\lambda = \frac{2\varepsilon_0 V_0}{\pi} \int_1^{R/g} \frac{dy}{\sqrt{y^2 - 1}} = \frac{2\varepsilon_0 V_0}{\pi} \log \frac{4R}{g} \tag{6}$$

The total charge q is found by multiplying λ by $(h + w)$. The surface capacitance is then

$$C_{surf} = \frac{q}{V_0} = \frac{2\varepsilon_0(h+w)}{\pi} \log \frac{4R}{g} \tag{7}$$

The total capacitance is therefore the sum of the gap and surface capacitances, $C_T = C_{gap} + C_{surf}$. Because C_T is inversely proportional to the gap width g, we obtain $f_{res} \propto \sqrt{g}$.

The inductance of the ring is calculated as follows (2, 3):

$$L = \mu_0 R_m \left(\log \frac{8R_m}{h+w} - \frac{1}{2}\right) \tag{8}$$

where $R_m = R + w/2$ and ε_0 is the free-space permeability. For the 35-μm-gap case, $L = 0.91 \times 10^{-10}$ H and $C_T = 0.617$ fF reproduce the resonance frequency of 0.67 THz, which is very close to the simulated and experimentally measured one.
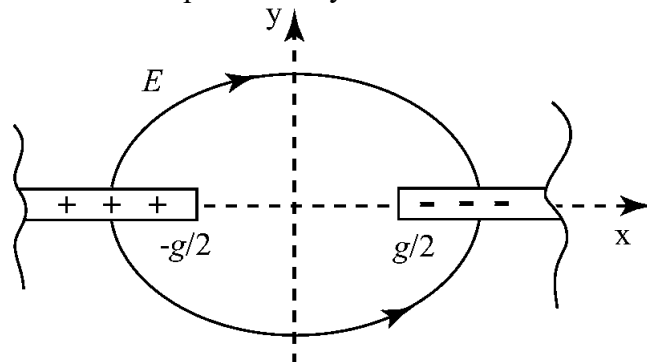

Figure S2. In the vicinity of the gap, the split ring looks like two semiplanes. The surface charge can be found using conformal mapping.

References

1. A. D. Wunsch, Complex Variables with Applications (Addison-Wesley, Reading, MA, 1983).
2. F. W. Grover, Inductance Calculations: Working Formulas and Tables (Instrument Society of America, Research Triangle Park, NC, 1981).
3. O. Sydoruk, E. Tatartschuk, E. Shamonina, and L. Solymar, Analytical formulation for the resonant frequency of split rings. *J. Appl. Phys*. **105**, 014903 (2009).